This is the author's version of an article that has been published in this journal. Changes were made to this version by the publisher prior to publication.
The final version of record is available at http://dx.doi.org/10.1109/TPWRD.2016.2545922

Advanced modeling of magnetic cores for damping of high frequency power system transients

Marcin Szewczyk, *Senior Member, IEEE*, Kamil Kutorasiński, Jarosław Pawłowski, Wojciech Piasecki, *Member, IEEE*, Marek Florkowski, *Senior Member, IEEE*

***Abstract*— This paper presents novel approach to modeling of magnetic cores for high frequency transient analyses in power system applications. A method is presented of obtaining frequency dependent, nonlinear equivalent circuit model of magnetic cores, suitable for simulations of transients in high frequency and high current conditions. The model can be used in any EMTP-like simulation software for power system transient analyses and hardware design of transient mitigation solutions. The model has been developed based on the frequency characteristics of the complex impedance of a magnetic core, measured for different operating points on the magnetization curve. Based on the measured characteristics and on some basic material properties, a nonlinear equivalent model composed of a set of lumped elements was established. The presented method is generic, however, the results are presented for a magnetic core of nanocrystalline type and the model implementation is shown in EMTP simulation software. The exemplary model is dedicated for the frequency range $f = 1\,\mathrm{kHz} \div 100\,\mathrm{MHz}$, and for the current range $I = 0 \div 10\,\mathrm{kA}$. The model accuracy was validated with selected measurement results and the accuracy of the method is thoroughly discussed.**

***Index Terms*— Frequency dependence, magnetic cores, modeling, power system transients, saturation effect, simulations.**

I. Introduction

A. Damping of power system transients with magnetic cores

High frequency transient phenomena originating from switching operations pose risk to power equipment. Filtering of high $\mathrm{d}u/\mathrm{d}t$ or high $\mathrm{d}i/\mathrm{d}t$ transients can effectively be achieved by using high frequency magnetic cores comprising ferrites, amorphous, or nanocrystalline materials. Application areas for such cores include switching of inductive loads with Vacuum Circuit Breakers (VCB) [1], [2], or operations of Gas-Insulated Switchgear (GIS) disconnectors [3], [4], [5]. Optimization of particular solution's design requires transients studies using appropriate equivalent models of the magnetic cores. The models should reflect the core behavior over broad frequency and current ranges.

The concept of using magnetic cores for mitigation of power system transients was first introduced in a practical industrial application for MV systems, to protect arc furnace transformers from transients originating from operations of VCB [1]. For this application, the filtering cores, typically coupled with a shunt resistor, are introduced in series to the main current path. The inductance of the core is selected to dominate the inductance of the system between the VCB and the transformer, so that the core takes over the oscillations occurring due to the transfer of the magnetic energy trapped in the inductive element to the capacitances of the system (e.g. cable in [1]), and the shunt resistor coupled to the core is selected to control the oscillating character of the system. The core is typically modeled by a two-terminal circuit consisting of inductor and resistor elements connected in parallel [2]. The impedance of the model is close to zero at $50/60\,\mathrm{Hz}$, while for higher frequencies the impedance is almost purely resistive. The travelling waves reflections are avoided by selection of the high frequency impedance so that its value is close to the surge impedance of the system.

Using magnetic cores for mitigation of transients originating from operations of GIS disconnectors is one of the concepts that is currently being under development for application in EHV and UHV class GIS. The cores of ferrite [6], [7], [8], amorphous [4], and nanocrystalline [4], [9] type are placed directly on the GIS conductor. Physical mechanisms responsible for transients mitigation include eddy current- and magnetization- losses [4], [9]. These mechanisms are both frequency- and saturation-dependent [10]. According to e.g. [4], [11], [12] the saturation effect of the material magnetization characteristics is an important factor leading to substantial reduction of transients attenuation effectiveness.

State-of-the-art methods on modeling of magnetic cores for mitigation of transients in GIS are reviewed in [3], where also a new magnetic core model is introduced for mitigation of Very Fast Transient Overvoltages (VFTO) originating from the GIS disconnector operations. The simplistic modeling approach, using linear inductor and resistor connected in parallel, is described e.g. in [6]. The method reported in [13] includes the

M. Szewczyk, W. Piasecki, M. Florkowski are with ABB Corporate Research Center, 31-038 Krakow, Starowislna 13A, Poland (e-mail: marcin.szewczyk@pl.abb.com, wojciech.piasecki@pl.abb.com, marek.florkowski@pl.abb.com).

K. Kutorasiński is with ABB Transformer Technology Center, Łódź, Poland (e-mail: kamil.kutorasinski@pl.abb.com).

J. Pawłowski is with AGH University of Science and Technology, Faculty of Physics and Applied Computer Science, 30-059 Kraków, Mickiewicza 30, Poland (e-mail: jaroslaw.pawlowski@fis.agh.edu.pl).

Corresponding author: M. Szewczyk (e-mail: marcin.szewczyk@pl.abb.com).

Color versions of one or more of the figures in this paper are available online at http://ieeexplore.ieee.org material frequency dependent characteristics, however without inclusion of saturation effect. The method is qualitatively applied in [13] to assess its applicability by comparison of the attenuation results with selected results from [6]. The method reported in [11] includes saturation effect in analytical formulas, indicating that the saturation effect is an important factor influencing the transient mitigation overall effectiveness.

The model introduced in [3] combines low-current frequency characteristics of the cores with the saturation effect. The saturation effect is modeled in [3] in a simplistic way, as a bypass branch short-circuiting the frequency dependent part of the model at a certain saturation current value. The saturation current is calculated according to the magnetic material properties assumed for the main frequency component of the transient voltage waveform.

B. *Paper aim and structure*

This paper presents a new method of modeling of magnetic cores (rings) by representing their magnetic nonlinear properties both in high frequency f and high current I conditions, where standard models (low frequency and linear) are not applicable. The model introduced here is a step forward as compared to the model reported in [3]. The new model involves frequency characteristics of the core modeled at any given range of both frequency and current, as related to particular transient conditions.

The methodology presented in this paper allows one to develop a lumped element equivalent circuit model which can be implemented in any transient simulation software, e.g. EMTP [14]. The model can be then applied for system studies as well as for hardware design of transient mitigation solutions that are based on energy dissipation in magnetic cores.

The paper is organized as follows: Section I gives a general outline of the method presented, together with the indication on the method possible application area. Section II presents an overview of the modeling method introduced in the present paper. Section III presents the input data needed for the model development, with primary focus on the measurement method used to obtain frequency and current dependent impedance characteristics. Measurement results used for the model identification are also shown. Section IV introduces the method of the model development, giving the detailed description on how to transfer the measured impedance characteristics into a complete frequency dependent and nonlinear model. Implementation of the model in any EMTP-like simulation software is presented as well. Section V provides the method validation with selected measurement and simulation results in frequency- and time- domains, for different frequency and current conditions. Section VI presents a discussion of the method limitations and main sources of the method inaccuracy. Section VII offers summary and conclusions.

II. Method Overview

The method of modeling of magnetic cores here presented is based on the frequency characteristics of the magnetic core complex impedance Z measured for different operating points on the magnetization curve $B(H)$. In addition to the measured characteristics, only basic material parameters of magnetic cores are used, as typically provided by the material manufacturers, such as the core geometry, relative permeability for low frequency (typically e.g. 10 kHz), electrical conductivity ($\sim 100\,\mu\Omega\cdot$cm), etc. For the core used in this paper, the following geometry parameters apply: magnetic path length $l_{\mathrm{B}} = 0.588$ m, effective cross-sectional area $A_{\mathrm{e}} = 2.78$ cm^2.

The impedance Z of the core is measured in a set-up where different operating points on the core magnetization curve $B(H)$ can be selected by the bias current I_{dc}, which introduces to the magnetic core the corresponding bias field $H_{\mathrm{dc}}(I_{\mathrm{dc}})$. The overall impedance characteristics are thus formed by a set of functions measured for n values of the bias current I_{dc}, namely: $Z = Z(f, I_n)$, where I_n denotes different values of I_{dc}.

Based on the measured set of $Z(f, I_n)$, n linear, frequency dependent equivalent models composed of k resistive and inductive lumped elements $R_k L_k$ are established. By that means, for each operating point on the magnetization characteristics $B[(H(I_n)]$ a model of $Z(f, I_n)$ is established.

Finally, the set of $Z(f, I_n)$ reproduced by the set of n linear circuits, each of which composed of k resistive and inductive elements $R_k L_k$, are combined to compose one frequency dependent and nonlinear equivalent circuit representing the magnetic core high frequency behavior in high current conditions. Such model represents the frequency dependence of inductive and resistive behavior of the core as well as the saturation effects of both of these quantities.

III. Measurement of Magnetic Core Impedance in Frequency Domain and High Current Conditions

A. *Measurement method*

Fig. 1 illustrates the electric circuit used for measuring of $Z(f, I_n)$ characteristics. The circuit consists of two magnetic cores of the same type with a primary ac winding used for ac magnetization with the current I_{ac}, and a supplementary dc winding in which the bias current I_{dc} generates the bias field H_{dc}. The dc bias current is used to magnetize the cores and thus to control the cores operating point on the magnetization curve while measuring the core frequency characteristics.

The method of measuring ac magnetization with the dc bias field is typically used for designing of e.g. dc biased chokes [15]. The two-cores arrangement shown in Fig. 1 ensures that the ac current $I(\phi_{\mathrm{ac}})$ corresponding to the ac magnetization is cancelled in the supplementary dc winding. This ensures that the dc circuit impact on the ac current measurement is avoided.

Measurement of the complex impedance $Z(f, I_n)$ over a given frequency range is performed using a network analyzer. The magnetic core impedance in general depends on the operating point on its magnetization characteristics $B(H)$, which in our set-up is controlled by the bias current I_{dc}. To include this effect we thus measured the $Z(f, I_n)$ characteristics for $n = 14$ values of the I_{dc} current, namely for: I_n = 0, 1, 3, 5, 7, 11, 14, 17, 20, 25, 30, 40, 50 A. Further in the paper we denote this discrete set of values as the current range $I_n = 0 \div 50$ A.

This is the author's version of an article that has been published in this journal. Changes were made to this version by the publisher prior to publication.
The final version of record is available at http://dx.doi.org/10.1109/TPWRD.2016.2545922

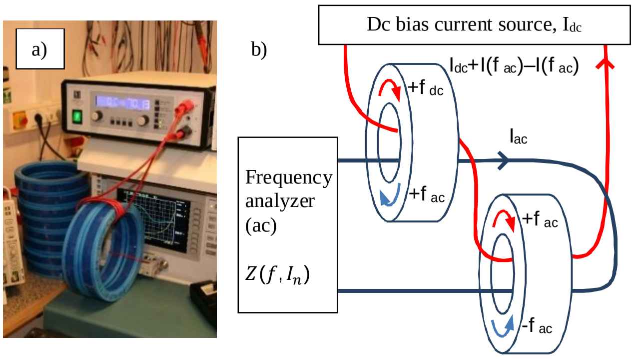

Fig. 1 Illustration of the circuit used for the measurement of impedance $Z(f, I_n)$ of a pair of magnetic cores, measured for n different values of the bias current I_{dc}, denoted in text as I_n; a) physical set-up with example of magnetic core and network analyzer Agilent 4294A, b) block diagram.

The I_n range was selected to reach the saturation level of $Z(f, I_n)$ for a given core material and geometry used in this study. Fig. 2 shows the magnetization curves $B(H)$ of the nanocrystalline cores of exemplary types, as per [2]. It can be seen that the cores with lower initial rise of $B(H)$ curve (lower initial relative permeability μ_r) require higher currents to achieve the nonlinear range $B(H)$ and then to saturate. It should also be noted, that the measurement of $Z(f, I_n)$ should include the whole range of $B[H(I_n)]$, and thus high values of I_n should be employed (e.g. up to $I_n = H_n l_B = 200 \cdot 0.588 = 340$ A for the Core 3 in Fig. 2).

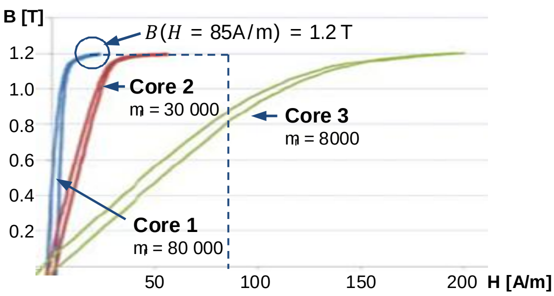

Fig. 2 Magnetization curves $B(H)$ as per [16] (blue: *Core 1* type used in this work, red: *Core 2*, green: *Core 3*), where range of $H_n = I_n / l_B = \frac{0 \div 50\ \mathrm{A}}{0.588\ \mathrm{m}} = 0 \div 85\ \mathrm{A/m}$ is indicated by dashed line

Moreover, the $B(H)$ curve should be extrapolated to the H values corresponding to the maximum instantaneous values of the current occurring in the system where the cores are used. In the exemplary application, where attenuation of VFTO in GIS is considered, the magnetic cores are used to dissipate energy of the VFTO travelling waves (e.g. in [3], [4]). In this case, the instantaneous values of the current can reach 10 kA [17], which for the core used in this study corresponds to $H = 10\mathrm{kA}/0.588\ \mathrm{m} = 17\ \mathrm{kA/m}$. The aspect of the model extrapolation up to 10 kA is further discussed in Section III. Measurements presented in this paper were conducted for an exemplary core indicated in Fig. 2 as Core 1.

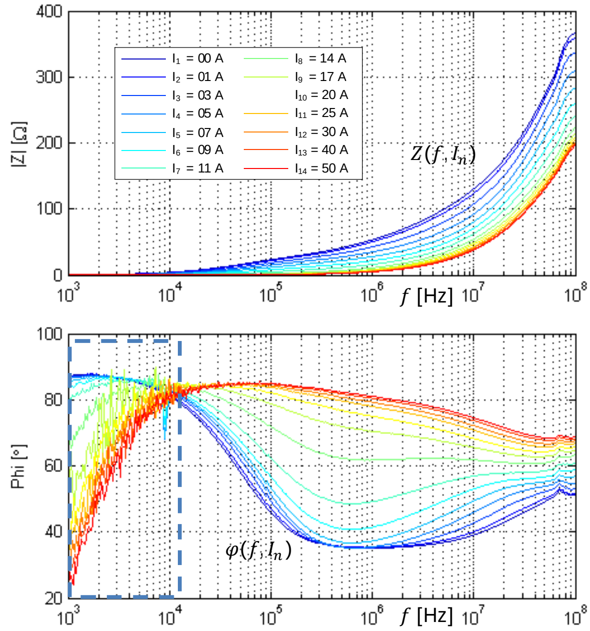

Fig. 3 Measured $Z(f, I_n)$ characteristics: a) the absolute value $|Z|(f, I_n)$ and b) the phase angle $\varphi(f, I_n)$, for a set of two cores in a set-up shown in Fig. 1, of type *Core 1* as per Fig. 2, for 14 values of $I_n = 0 \div 50$ A; colors in both figures (a) and (b) denote bias current according to legend in figure (a).

B. *Measured $Z(f, I_n)$ characteristics*

The inductive behavior and the magnetic losses of the core material are described with the complex core impedance. It is represented by the absolute value $|Z|(f, I_n)$ and the phase angle $\varphi(f, I_n)$. Fig. 3 shows the set of characteristics $Z(f, I_n)$ measured in the set-up shown in Fig. 1, where $I_n = 0 \div 50$ A as defined in Section II.A (lower values in Fig. 3a and lower values for higher frequencies in Fig. 3b are for higher bias currents). The corresponding field $H_n = I_n / l_B = 0, \dots, 85$ A/m).

C. *Discussion on measured $Z(f, I_n)$ characteristics*

1) *Low frequency behavior of $\varphi(f, I_n)$*

For the low frequency region the core exhibits almost purely inductive character, which is equivalent to: $\varphi(f, I_n) \to 90$ deg and $|Z|(f, I_n) \to 0\ \Omega$. It can be seen in Fig. 3 that at low frequencies in the range of $f \approx 1$ kHz $\div$ 10 kHz (boxed in Fig. 3), the phase angle $\varphi(f, I_n)$ is subject to significant measuring error (which further increases with the core saturation, i.e. for higher values of I_n). This can be explained with the simple series model of magnetic core impedance:

$$Z = R_S + j\omega L_S, \qquad (1)$$

with the series resistance R_S and the series inductance L_S defined at a given frequency $f = \omega / 2\pi$ by the real and imaginary parts of $Z(f, I_n)$ respectively:

$$\begin{aligned} R_S(f, I_n) &= Re[Z(f, I_n)] \\ L_S(f, I_n) &= Im[Z(f, I_n)]\omega^{-1}. \end{aligned} \qquad (2)$$

As the measured phase angle $\varphi(f, I_n)$ is given by the formula:

$$\tan\varphi = \frac{\omega(L_S + L_c)}{R_S + R_c} \qquad (3)$$

where R_S and L_S are defined by (1), R_c and L_c represent the resistance and the inductance of the connecting wires respectively. It implies that for $f \to 0$, the $\tan\varphi$ becomes very sensitive to the change of either denominator or numerator (as both of them go to zero for $f \to 0$, as shown in Fig. 3). In consequence, the resistance R_c in (3) has an increasing share in the overall resistance measured.

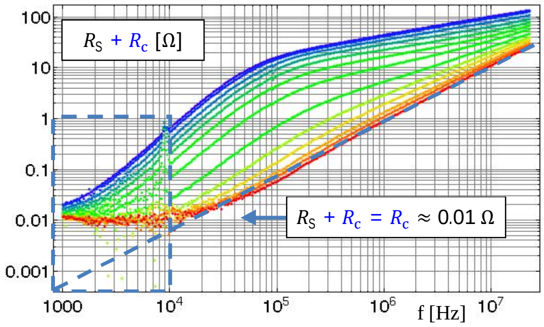

Fig. 4 Frequency characteristics of measured resistance $R_S + R_c$ in loglog scale; box indicates the area where $R_c = 0.01\ \Omega$ becomes significant (interpreted as the resistance of connecting wires); line indicates the core pure resistance (without wires) converging to 0; colors denote bias current according to legend in Fig 3.

Fig. 4 shows the measured resistance $R_S + R_c$ calculated according to (2) based on data shown in Fig. 3 (lower values are for higher bias currents). In Fig. 4 the frequency range 1 kHz ÷ 10 kHz where the $\varphi(f, I_n)$ does not converge to 90 deg is boxed, indicating the region where $R_S + R_c$ converges to the value of $\approx 0.01\ \Omega$. This value can be interpreted as a resistance of the connecting wires R_c (which has been confirmed by a separated dc resistance measurement). Slope-line in Fig. 4 indicates that for $f \to 0$ the core pure resistance (with no wires) converges to 0. In further steps in this paper we thus extrapolate the $\varphi(f, I_n)$ characteristics (shown in Fig. 3) in the region of 1 kHz ÷ 10 kHz, so that they converge to 90 deg.

2) High frequency behavior of $|Z|(f, I_n)$ and $\varphi(f, I_n)$

In Fig. 3 it can be seen that with the frequency increase, $\varphi(f, I_n)$ decreases and $|Z|(f, I_n)$ increases, which is due to the increase of resistive losses (eddy current and hysteresis) in high frequency region.

3) High current behavior of $|Z|(f, I_n)$ and $\varphi(f, I_n)$

Fig. 3 shows that with the current I_n increase, the absolute value $|Z|(f, I_n)$ decreases and the phase angle $\varphi(f, I_n)$ increases. Thus, the inductance of the core significantly decreases, but at the same time L_S becomes predominant over the resistance. Assuming the series model of the magnetic core impedance given by (1), it can be explained that with the current increase the resistance R_S at specific frequency decreases faster than the inductive reactance ωL_S. It means that with the current increase, the character of the impedance for a given frequency becomes more inductive. It has to be noted that at the frequency of 10 MHz the inductance of 0.3 μH (which is a realistic estimation of the inductance of the connecting wire) represents a reactive impedance of 20 Ω.

4) Saturation effect of $|Z|(f, I_n)$ and $\varphi(f, I_n)$

Fig. 2 and Fig. 3 show that for the maximum current value $I_n = 50$ A the core is almost saturated. Fig. 2 shows the saturation even below $H_n = 85$ A/m (which is equivalent to $I_n = 50$ A), and Fig. 3 shows almost no change in $Z(f, I_n)$ characteristics between $I_n = 40$ A and $I_n = 50$ A (red lines in Fig. 3).

IV. Model development

The process of the model development, as described in this section, is divided into 5 steps, as illustrated also in Fig. 6 and Fig. 7. Final model structure is shown in Fig. 8.

A. Linear models of individual $Z(f, I_n)$

Step 1: Each of the characteristics $Z(f, I_n)$ measured for a given current I_n (as shown in Fig. 3) is represented by a set of k resistive and inductive linear lumped elements $R_{n,k}L_{n,k}$:

$$Z(f, I_n) \to R_{n,k}L_{n,k} = R_k(I_n)L_k(I_n) \qquad (4)$$

The models composed of the $R_{n,k}L_{n,k}$ elements have the same structure for every $Z(f, I_n)$, as illustrated in Fig. 5. The number k of elements used in the models allows one to reproduce the measured characteristics $Z(f, I_n)$ with required accuracy. An exemplary method of identification of the model parameters $R_{n,k}L_{n,k}$ for a given I_n is presented in [18]. It allows to identify an analytical function $Z(s, I_n)$ in s-domain, which frequency characteristics matches with the measured one: $Z(f, I_n) \to Z(s, I_n)$, and then to represent the $Z(s, I_n)$ as a rational function of the complex frequency $s \equiv j\omega$ with real coefficients of its nominator $\{a_p\}$ and denominator $\{b_q\}$. As the rational function has real coefficients, it can be transferred into the form of a partial fraction decomposition:

$$Z(s, I_n) = \frac{a_p s^p + a_{p-1}s^{p-1} + \cdots + a_1 s + a_0}{b_q s^q + b_{q-1}s^{q-1} + \cdots + b_1 s + b_0} = \\ = R_0 + \sum_{k=1}^{k_{\max}} \frac{R_{n,k}s}{R_{n,k}/L_{n,k} + s} \qquad (5)$$

where n denotes current I_n ($n = 1,\ldots,14$ in our case) and k denotes the number of $R_{n,k}L_{n,k}$ elements for each I_n ($k = 0,\ldots,k_{\max}$).

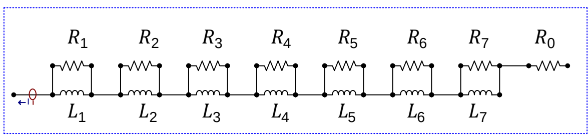

Fig. 5 Equivalent model of frequency dependent core impedance $Z(f, I_n)$ for a given current I_n.

The partial fraction decomposition given by (5) provides direct input to the Foster method of Lumped Element Equivalent Circuit (LEEC) synthesis [19] being represented by the equivalent circuit model $R_{n,k}L_{n,k}$, as shown in Fig. 5, as illustrating the model of Core 1 obtained for any given current I_n and consisting of $k = 0,\dots,7$ elements. The element R_0 in (5) and in Fig. 5 has negligible value in practice and as such it has not been included in the final model.

B. *Nonlinear model of all* $Z(f, I_n = 0 \div 50\text{A}, 10\text{kA})$

Step 2: For every k in the model obtained in Step 1, the $R_k(I_n)$ and $L_k(I_n)$ are interpolated with smooth analytical functions of $R_k(I)$ and $L_k(I)$ respectively:

$$\begin{aligned} R_k(I_n) &\rightarrow R_k(I) \\ L_k(I_n) &\rightarrow L_k(I) \end{aligned} \tag{6}$$

so that they can be integrated over I in the next step. The interpolation (e.g. spline) can be done in the range where the measurements of $Z(f, I_n)$ are conducted (in our case for $I_n = 0 \div 50$ A).

Step 3: The $R_k(I)$ and $L_k(I)$ given by (6) are integrated over I to obtain the corresponding voltage $U_k(I)$ and flux $\Phi_k(I)$ respectively:

$$\begin{aligned} R_k(I) &= \frac{dU_k(I)}{dI} \Rightarrow U_k(I) = \int_0^I R_k(\xi)d\xi \\ L_k(I) &= \frac{d\Phi_k(I)}{dI} \Rightarrow \Phi_k(I) = \int_0^I L_k(\xi)d\xi \end{aligned} \tag{7}$$

The $U_k(I)$ and $\Phi_k(I)$ are required for implementation of the model in EMTP-ATP simulation software [14] where the nonlinear characteristics of $R_k(I)$ and $L_k(I)$ elements are defined through $U_k(I)$ and $\Phi_k(I)$ respectively.

Step 4: The $U_k(I)$ and $\Phi_k(I)$ obtained in Step 3 are defined in the current range of $I \leq 50$ A (in our case), however the model needs to be valid also for higher currents (e.g. up to $I = 10$ kA as corresponding to VFTO conditions in GIS). The $U_k(I)$ and $\Phi_k(I)$ are thus extrapolated for the current I larger then the maximum current used in the measurements of $Z(f, I_n)$ (i.e. in our case for $I > 50$ A). For this purpose, a matching functions were used:

$$\begin{aligned} g(I) &= a_{\mathrm{g}} \cdot \mathrm{atan}(b_{\mathrm{g}} I) \\ h(I) &= a_{\mathrm{h}} \cdot \mathrm{atan}(b_{\mathrm{h}} I) \end{aligned} \tag{8}$$

where the parameters $a_{\mathrm{g/h}}$ and $b_{\mathrm{g/h}}$ were adjusted to ensure smooth fit of $g(I)$ with $U_k(I)$ and $h(I)$ with $\Phi_k(I)$, in the current range $I = 40 \div 50$ A. The resultant $U_k(I)$ and $\Phi_k(I)$ consist of two parts. One part is in the current range $I \leq 50$ A, where the data from measurements are used to calculate $U_k(I)$ and $\Phi_k(I)$ through integration of $R_k(I)$ and $L_k(I)$ respectively. Second part is in the current range $I \geq 50$ A, where the extrapolating functions $g(I)$ and $h(I)$ are matched to ensure smooth fit of the functions in the current range $I = 40 \div 50$ A. This approach gives physical behavior of the model up to 10 kA, which ensures that the model saturates for large currents I.

It can be seen in Fig. 7 that the $g(I)$ and $h(I)$ functions do not work in the current range of $I < 40$ A (the red dashed line does not match with the blue circles). Thus, these functions cannot be used in the whole current range.

Step 5: The $U_k(I)$ and $\Phi_k(I)$ obtained in Step 4 are discretized in the whole current range $I = 0 \div 10$ kA:

$$\begin{aligned} U_k(I) &\rightarrow U_k(I_{n'}) \\ \Phi_k(I) &\rightarrow L_k(I_{n'}) \end{aligned} \tag{9}$$

where the set of discrete current values $I_{n'}$ was selected as an exponential function of index n', namely $I_{n'} = \exp(n'/3)$. This ensures that the discrete functions $U_k(I_{n'})$ and $L_k(I_{n'})$ cover both regions of $U_k(I)$ and $\Phi_k(I)$: with rapid rate of change at $I \leq 50$ A and with slow rate of change at large currents $I > 50$ A (up to $I = 10$ kA).

The discrete values of $U_k(I_{n'})$ and $\Phi_k(I_{n'})$ are directly used in the EMTP simulation software [14]. The characteristics implemented in the software are limited to approximately 30 points, between which the software uses linear interpolation.

In Fig. 6 and Fig. 7 the discrete and the continuous values corresponding to the description given in Steps 1-5 above (for $k = 5$ elements) are shown in circles and lines respectively.

V. Model Validation

For the model validation, the equivalent inductance of the magnetic core series model (denoted further as the series inductance L_{S}) was analyzed in the frequency and the time domains.

A. *Validation in frequency-domain*

In the frequency domain, two series inductances were calculated according to (2), for three values of current: $I_n = 0, 11, 50$ A, and for the frequency range $f = 1$ kHz $\div$ 100 MHz. The $L_{\mathrm{S}}^{\mathrm{exp}}(f, I_n)$ was calculated based on the measured $Z(f, I_n)$ shown in Fig. 3. The $L_{\mathrm{S}}^{\mathrm{model}}(f, I_n)$ was calculated based on the model given by (5).

Fig. 9 shows the calculated inductances: $L_{\mathrm{S}}^{\mathrm{exp}}(f, I_n)$ (dots) and $L_{\mathrm{S}}^{\mathrm{model}}(f, I_n)$ (lines). It can be seen in Fig. 9 that at low frequencies the $L_{\mathrm{S}}^{\mathrm{exp}}(f, I_n)$ values are scattered around the values of $L_{\mathrm{S}}^{\mathrm{model}}(f, I_n)$. This is caused by the error in the phase angle measurement as seen in Fig. 3 and discussed in Section 2.C. Despite this discrepancy at low frequencies, good overall agreement between $L_{\mathrm{S}}^{\mathrm{exp}}(f, I_n)$ and $L_{\mathrm{S}}^{\mathrm{model}}(f, I_n)$ was achieved.

B. *Validation in time-domain*

For the model validation in the time domain, test set-up shown in Fig. 8 was used, where the magnetic core model was subjected to the input current $i(t)$ defined at a given frequency f by:

$$i(t) = I_{\mathrm{m}}(t) sin(2\pi f t) \tag{11}$$

where: $I_{\mathrm{m}}(t) = \alpha \cdot t$ is the time varying amplitude (with $\alpha = \mathrm{const}$). The amplitude $I_{\mathrm{m}}(t)$ raises linearly with time t, starting from $I(t = 0) = 0$ A up to $I(t_{\max}) = 50$ A. This makes the magnetic core model operating in its nonlinear mode and allows one to observe the model's hysteresis loop.

For analyzing the hysteresis loop, the voltage $v(t)$ across the model (see Fig. 8) was simulated. The hysteresis loop is given by the Faraday and the Ampere laws:

$$v(t) = -\frac{d(\Phi = BA_\mathrm{e})}{dt} \Rightarrow B(t) = \frac{-1}{A_\mathrm{e}}\int v(t)dt$$
$$i(t) = H(t)l_\mathrm{B} \Rightarrow H(t) = \frac{i(t)}{l_\mathrm{B}} \tag{12}$$

where A_e is the cross-sectional area of the core, l_B is the magnetic path length of the core, $i(t)$ is the input current given by (11), $v(t)$ is the voltage across the core model as indicated in Fig. 8 (since the core is wound with single turn, the number of turns was skipped as equal to unity).

Fig. 10 shows the input current $i(t)$ (red) and the voltage $v(t)$ across the core model, simulated in the model shown in Fig. 8 for both cases as specified above.

Fig. 11 shows hysteresis loops, calculated for the both cases, with indicated series inductances $L_\mathrm{S}(I)$, as read from the hysteresis slopes according to:

$$L_\mathrm{S}(I) = \frac{\mathrm{d}\Phi(I)}{\mathrm{d}I} = \frac{\mathrm{d}}{\mathrm{d}I}\int v(t)dt, \tag{13}$$

where $v(t)$ is the voltage across the core caused by the time derivative of the magnetic flux density $\Phi(I)$.

Fig. 11 illustrates the increase of the hysteresis width for higher frequency (thin loop for $1\ \mathrm{kHz}$ and thick for $1\ \mathrm{MHz}$). The dependence of the hysteresis width on the magnetic flux $\Phi(I)$ is visible also (for higher Φ, the width is lower).

In Fig. 11 the L_S values are indicated as read from the hysteresis slopes for three current values: $I_n = 0, 11, 50\ \mathrm{A}$. By comparing Fig. 11 and Fig. 9 it can be seen that that the L_S read from the hysteresis loops in Fig. 11 are in agreement with those calculated in Fig. 9, for both frequencies: $f = 1\ \mathrm{kHz}$ and $f = 1\ \mathrm{MHz}$.

It can be thus concluded, that L_S read from the hysteresis are in good agreement with the measured ones. Other aspect of validation is related to the series resistance R_S, which can be done by comparison of the simulated hysteresis loops width with the measured ones.

The saturation flux density can be read from Fig. 11a: as $B_\mathrm{sat} = \frac{\Phi_\mathrm{sat}(50\mathrm{A})}{2(A_\mathrm{e}\cdot p)} = \frac{0.47\ \mathrm{V\cdot s}}{2\cdot 2.78\cdot 10^{-4}\cdot 0.73\ \mathrm{m}^2} = 1.16\ \mathrm{T}$, where $2\mathrm{A_e}$ is a geometrical cross-sectional area of two cores in Fig. 1 and p is the filling factor defining of the fraction of the core cross section area occupied by the magnetic material. The value $B_\mathrm{sat} = 1.16\ \mathrm{T}$ is in a good agreement with the manufacturer data [16], where $B_\mathrm{sat} \approx 1.2\ \mathrm{T}$ (see also Fig. 2). Fig. 2 shows, that for $I_n = 50\ \mathrm{A}$ (for which the corresponding magnetic strength is $H_n = \frac{I_n}{l_\mathrm{B}} = \frac{50\ \mathrm{A}}{0.588\ \mathrm{m}} = 85\ \frac{\mathrm{A}}{\mathrm{m}}$), the saturation already occurred, and the value of the magnetic flux density is $B[H(I = 50\mathrm{A}) = 85\ \mathrm{A/m}] = B_\mathrm{sat} = 1.2\ \mathrm{T}$.

VI. Discussion on Method Limitations and Sources of Inaccuracy

The following are possible sources of the method limitations and inaccuracy.

The model of the core impedance shown in Fig. 5, is composed of L and R elements that represent any impedance of inductive-resistive character. This implies that the particular model structure shown in Fig. 5 is applicable for the impedance with the phase angle between 0 and 90 deg, as measured in the present paper (see Fig. 3). In the present paper, the impedance was measured within the range of currents covered with the available measurement set-up (i.e. up to 50 A), and then extrapolated towards higher currents. For the higher currents, it may be expected that the character of the cores impedance could change from inductive-resistive (as shown in Fig. 3) to capacitive-resistive one. In such case, the model structure would require to be extended to reflect capacitive-resistive character of the impedance. However, the overall method of identifying the nonlinear core model based on the measured impedance characteristics, as presented in this paper, is valid. The frequency characteristics of the cores impedance can potentially be affected by internal resonances occurring at specific current and frequency conditions beyond the experimental limits employed in the work presented. The presently evaluated model cannot account for that, however up to the current values used in the experiments such a fine structure of the characteristics was not observed.

Measuring the $Z(f, I_n)$ for relatively low current range (specifically not reaching the saturation region) can cause higher error of extrapolation in *Step IV* (see Section III). As seen in Fig. 2, for different materials different current levels are needed in order to reach the point of saturation. In our case, where *Core 1* was used, the current of $50\ \mathrm{A}$ was sufficient to reach the saturation region (see Fig. 2). It should be also noted that other functions than (8) can be used to give good extrapolation towards saturation. Also, when the measurements of $Z(f, I_n)$ are available for higher current range I_n, the extrapolation error caused by fitting (8) to (7) can be reduced. This is specifically of importance for those parts of the model (i.e. those $R_{n,k}L_{n,k}$ elements for given n), which has low rising slope, and thus require high current to properly reproduce their saturation.

It should be noticed, that the set of the $R_k(I)$ and $L_k(I)$ are obtained with particular error resulting from two sources. One source is the measurement error of obtaining $Z(f, I_n)$ in Fig. 3. Second error comes from the method of approximation of $R_{n,k}L_{n,k}$ elements from $Z(f, I_n)$, see *Step 1* (Section III).

Moreover, the calculation of $\mathrm{U}_k(I)$ and $\Phi_k(I)$ requires that the $R_k(I)$ and $L_k(I)$ are integrated over I, see (7) in *Step 3* (see Section III). Errors cumulated in each step of the $R_k(I)$ and $L_k(I)$ integration can be limited by employing higher number n of $Z(f, I_n)$ characteristics measured.

VII. Summary and Conclusions

This paper presents a method on modeling of magnetic cores in high frequency and high current conditions. The method is based on the frequency characteristics of the magnetic cores impedance measured for different operating points on the cores magnetization characteristics.

The presented method is generic, however the results presented in the paper have been obtained and reported for a specific core. The model development process was described in step-by-step manner for the frequency range $f = 1\ \mathrm{kHz} \div 100\ \mathrm{MHz}$, and for the current range $I = 0 \div 50\ \mathrm{A}$ extrapolated to $10\ \mathrm{kA}$. According to the method, the model has been obtained for a pair of the magnetic cores of the given type.

The high current conditions imply applicability of the model for MV as well as HV products. The methodology here presented can be used to prepare tools for selecting and sizing of the magnetic cores in order to achieve the required damping effect of power system transients in MV or HV applications.

The accuracy of the method was discussed (see Section VI). To increase the model accuracy, the characteristics of $Z(f, I_n)$ should be measured for highest possible number of current I_n values (in this study, 14 values were measured).

The validation of the model has been shown in the frequency and the time domains for different frequency and current conditions (see Fig. 9 and Fig. 11). Good accuracy was demonstrated by analyzing the series inductance $L_S(f, I_n)$ for different values of I_n and frequencies, by comparison of the calculated values with the measured ones. Full validation of the model will require comparison of the model performance in specific transient conditions with equivalent experimental results.

VIII. References

[1] W. Piasecki, M. Fulczyk, M. Florkowski, P. Werle, O. Kouzmine, J. Szczechowski, “Mitigating VCB-induced very fast transients in industrial installations. Case study: arc furnace transformer”, *CIGRE 2011 Joined A2/D1 Colloquium*, Kyoto, 11-16.09.2011

[2] D. Smugala, W. Piasecki, M. Ostrogorska, M. Florkowski, M. Fulczyk, O. Granhaug, “Wind Turbine Transformers Protection Method Against High-Frequency Transients,” *IEEE Trans. Power Delivery*, vol. 30, No. 2, pp. 853-860, Apr. 2015.

[3] M. Szewczyk, J. Pawłowski, K. Kutorasiński, W. Piasecki, M. Florkowski, U. Straumann, “High Frequency Model of Magnetic Rings for Simulation of VFTO Damping in Gas-Insulated Switchgear with Full-scale Validation,” *IEEE Trans. Power Delivery*, vol. 30, No. 5, pp. 2331-2338, Oct. 2015.

[4] Y. Guan, G. Yue, W. Chen, Z. Li, W. Liu, “Experimental Research on Suppressing VFTO in GIS by Magnetic Rings,” *IEEE Trans. Power Delivery*, vol. 28, No. 4, pp. 2558-2565, Oct 2013.

[5] U. Riechert, M. Bösch, M. Szewczyk, W. Piasecki, J. Smajic, A. Shoory, S. Burow, S. Tenbohlen, “Mitigation of Very Fast Transient Overvoltages in Gas Insulated UHV Substations,” *44th CIGRÉ Session*, 2012.

[6] W. D. Liu, L. J. Jin, J. L. Qian, "Simulation test of suppressing VFT in GIS by ferrite rings," in Proc. 2001 International Symposium on Electrical Insulating Materials, pp. 245-247, Beijing, China, 2011.

[7] J. V. G. Rama Rao, J. Amarnath, S. Kamakshaiah, "Simulation and measurement of Very Fast Transient Overvoltages in a 245 kV GIS and research on suppressing method using ferrite rings," ARPN Journal of Engineering and Applied Sciences, vol. 5, no 5, pp. 88-95, May 2010.

[8] S. Burow, U. Riechert, W. Köhler, S. Tenbohlen, "New mitigation methods for transient overvoltages in gas insulated substations," in Proc. Stuttgarter Hochspannungssymposium, Stuttgart, Germany, 2012, pp. 169-181.

[9] S. Burow, U. Straumann, W. Köhler, S. Tenbohlen, “New Methods of Damping Very Fast Transient Overvoltages in Gas-Insulated Switchgear,” *IEEE Trans. Power Delivery*, vol. 29, No. 5, pp. 2332-2339, October 2014.

[10] D. J. Griffiths, “Introduction to Electrodynamics”, 3rd edition, *Prentice Hall*, 1999

[11] J. He, Y. Guan, W. Liu, W. Chen, Z. Li, "Design Optimization of Ferrite Rings for VFTO Mitigation," IEEE Trans. Power Delivery, 2014 (accepted for publication).

[12] S. Burow, S. Tenbohlen, W. Köhler, J. Smajic, A. Tröger, W. Holaus, "Can ferrite materials or resonant arrangements reduce the amplitudes of VFTO in GIS," in Proc. 2011 17th International Symposium on High Voltage Engineering, Hannover, Germany, 2011.

[13] Q. Li, M. Wu, "Simulation method for the applications of ferromagnetic materials in suppressing high-frequency transients within GIS," IEEE Trans. Power Delivery, vol. 22, no. 3, pp. 1628-1632, July 2007.

[14] H. W. Dommel, W. S. Meyer: “Computation of electromagnetic transients,” *Proceedings of the IEEE*, vol. 62, no. 7, July 1974, pp. 983-993.

[15] R. Hilzinger, W. Rodewald, “Magnetic Materials,” Publicis Publishing, Erlangen, 2013.

[16] Magnetec GmbH, “Product specification for inductive components,” [Online] (material data sheet). Available: www.magnetec.de, 2014.

[17] G. Ecklin and D. Schlicht, “Overvoltages in GIS caused by the operation of isolators,” in *Proc. 1979 of the Brown Boveri Research Centre*, Baden, Switzerland, September 3-4, 1979.

[18] M. Szewczyk, J. Pawłowski, K. Kutorasiński, S. Burow, S. Tenbohlen, W. Piasecki, “Identification of rational function in s-domain describing a magnetic material frequency characteristics,” *9th International Conference on Computation in Electromagnetics*, CEM 2014, 31 March - 1 April 2014, London, UK.

[19] J. Russer at al. “Equivalent Lumped Element Network Synthesis for Distributed Passive Microwave Circuits”, Microwave Review, Vol. 17, Issue: 2; Start page: 23; Date: 2011.

IX. Biographies

Marcin Szewczyk (M’2012–SM’2014), born in Koszalin, Poland, in 1974, received his M.Sc. and Ph.D. degrees in Electrical Engineering from Warsaw University of Technology, Poland, in 2000 and 2009 respectively. Since February 2010 he has been working as a researcher with ABB Corporate Research in Cracow, Poland. His research is mainly in the field of power system analyses and advanced simulations, transients analyses and transients mitigation, insulation coordination studies, 3D modeling and simulations of electromagnetic fields. (ABB Corporate Research, Starowislna 13A, 31-038 Krakow, Poland, E-mail: marcin.szewczyk@pl.abb.com). Dr. Szewczyk is a Senior Member of IEEE and Polish Society for Theoretical and Applied Electrical Engineering.

Kamil Kutorasiński was born in 1985, received his M.Sc. and Ph.D. degrees in physics from the University of Science and Technology (AGH) in Kraków. His research was in the field of transport properties calculation in advanced material based on *ab initio* DFT methods as well as FEM modelling and simulations of electromagnetic fields. Since 2015 he has been with ABB Transformer Technology Center in Poland.

Jarosław Pawłowski was born on 17 October 1985 in Krynica-Zdrój, Poland. He received his M.Sc. in Technical Physics from the AGH University of Science and Technology (Kraków, Poland). Recently, he received his PhD in spintronics at the same University. His research interests include modeling of single-electron nanodevices and non-linear effects in magnetic materials.

Wojciech Piasecki was born in Poland on May 15,1966. He received the M.Sc. degree in electronics from the University of Science and Technology, in Kraków Poland, Poland, and the Ph.D. degree from the Jagiellonian University, Kraków. He has been working for many years in electromagnetic and electrical phenomena, including high-frequency and nonlinear modeling of electrical equipment. Currently, he is a Researcher with the Corporate Research Center in Kraków. His main research concentrates around transient network phenomena analysis.

Marek Florkowski (M'97-SM'08) received the M.S. and Ph.D. degrees in electronics from AGH University of Science and Technology in Kraków in 1990 and 1994, respectively. From 1990 to 1992 he was employed at ABB Corporate Research Center in Baden-Dättwil. In 2009 he obtained habilitation. He is currently responsible for ABB Corporate Research in Krakow, Poland. A member of CIGRE, and APEE. He is chair of the Technical Committee on Diagnostics of the IEEE Dielectrics and Electrical Insulation Society.

This is the author's version of an article that has been published in this journal. Changes were made to this version by the publisher prior to publication.
The final version of record is available at http://dx.doi.org/10.1109/TPWRD.2016.2545922

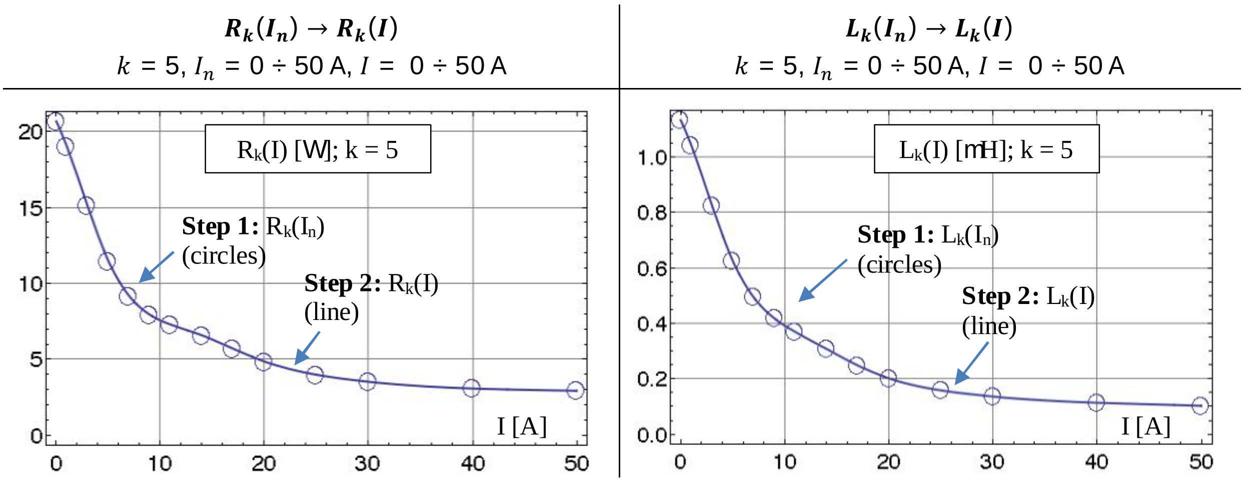

Fig. 6 Step-by-step process of model development according to description in Section III; *Step 1*: identification of $R_k(I_n)$ and $L_k(I_n)$ according to (4), *Step 2*: interpolation of $R_k(I_n)$ and $L_k(I_n)$ into $R_k(I)$ and $L_k(I)$ according to (6); for exemplary $R_{n,k}L_{n,k}$, where $k = 5$.

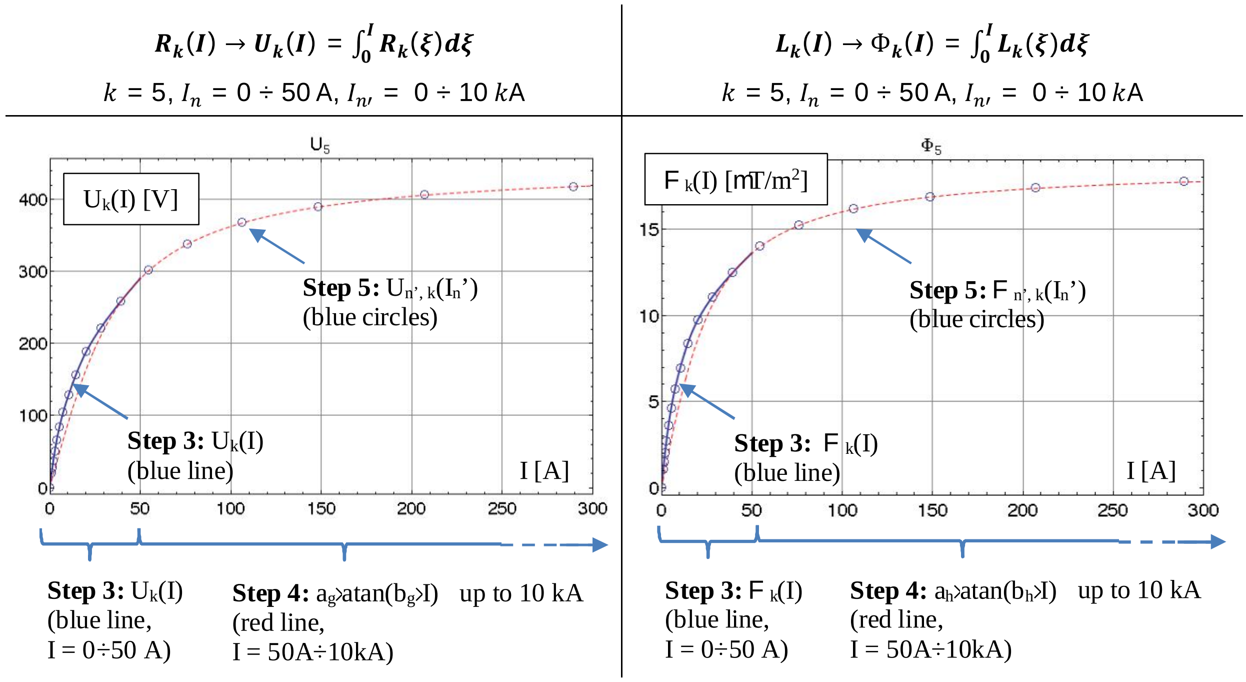

Fig. 7 Step-by-step process of model development according to description in Section III; *Step 3*: integration of $R_k(I)$ and $L_k(I)$ into $U_k(I)$ and $\Phi_k(I)$ according to (7), *Step 4*: extrapolation of $U_k(I)$ and $\Phi_k(I)$ according to (8), *Step 5*: discretization of $U_k(I)$ and $\Phi_k(I)$ into $U_k(I_{n'})$ and $\Phi_k(I_{n'})$; for exemplary $R_{n,k}L_{n,k}$, where $k = 5$.

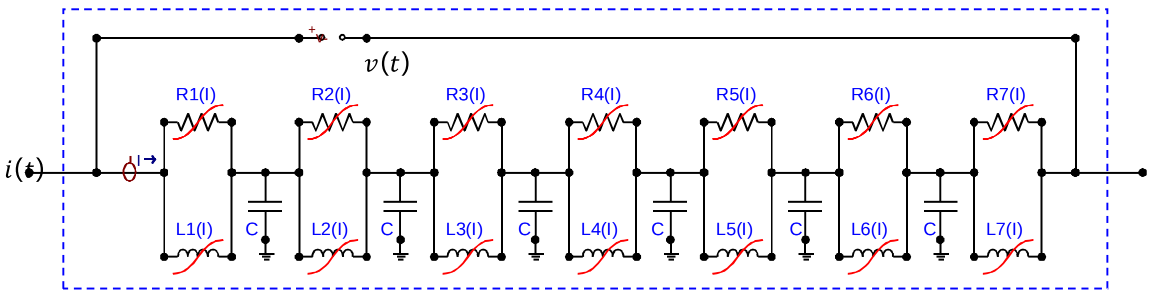

Fig. 8 Full model of a pair of magnetic cores shown in Fig. 1, for high frequency and high current conditions, including all of the $Z(f, I_n)$ characteristics shown in Fig. 3, developed according to description in Section III (negligible $C = 0.01$ pF added to avoid numerical issues).

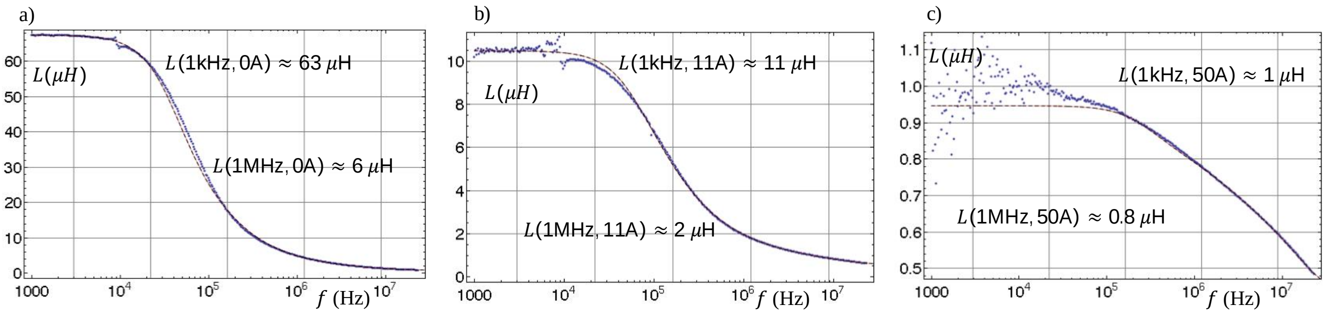

Fig. 9 Series inductances $L_s^{\exp}(f)$ and $L^{\text{model}}(f)$ calculated based on measured impedance $Z^{\exp}(f)$ (dots) and based on modeled impedance $Z^{\text{model}}(f)$ (dashed line); for I_n: a) 0 A, b) 11 A, c) 50 A; values of L_S are indicated for comparison with the corresponding L_S read from hysteresis loops shown in Fig. 11.

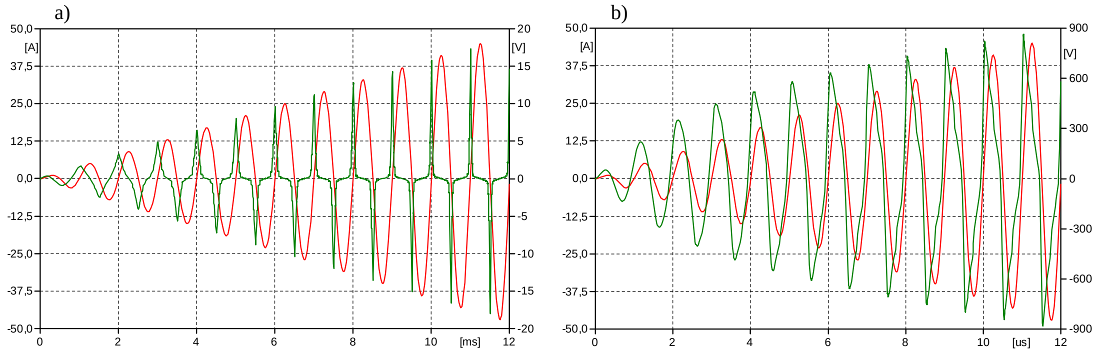

Fig. 10 Input current $i(t)$ (red) according to (11) and voltage $v(t)$ across the core model calculated for the model shown in Fig. 8, for two frequencies, as described in section IV: a) $f = 1$ kHz (*Case 1*), b) $f = 1$ MHz (*Case 2*).

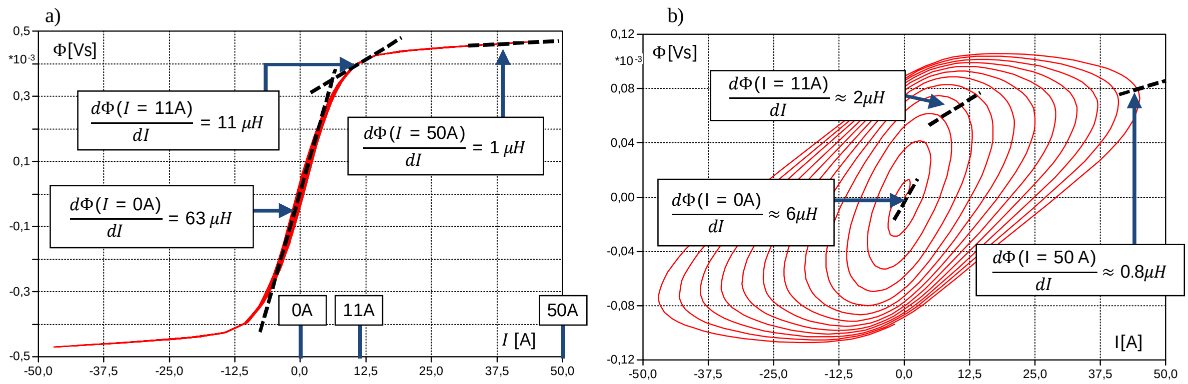

Fig. 11 Hysteresis loops calculated for the model shown in Fig. 8, for two frequencies, as described in section IV: a) $f = 1$ kHz (*Case 1*), b) $f = 1$ MHz (*Case 2*); the slopes $\mathrm{d}\Phi(\mathrm{I})/\mathrm{d}I$ serve for estimation of the series inductances $L_S(I)$ for $I_n = 0{,}11{,}50$ A; values of L_S are indicated for comparison with the corresponding L_S shown in Fig. 9.